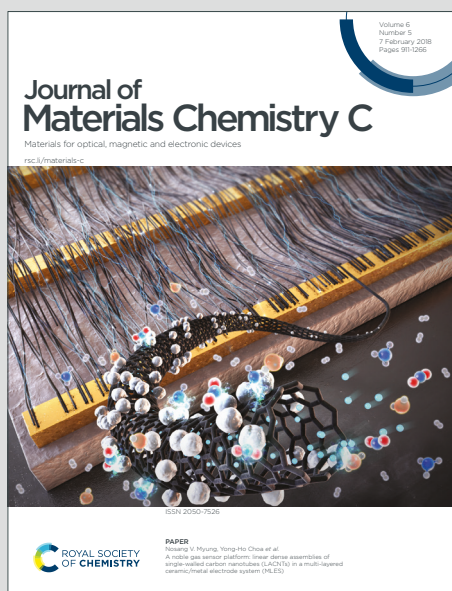


Journal of Materials Chemistry C

Materials for optical, magnetic and electronic devices

Accepted Manuscript

This article can be cited before page numbers have been issued, to do this please use: M. Shafikov, S. Tang, C. Larsen, M. Bodensteiner, V. N. Kozhevnikov and L. Edman, *J. Mater. Chem. C*, 2019, DOI: 10.1039/C9TC02930C.



This is an Accepted Manuscript, which has been through the Royal Society of Chemistry peer review process and has been accepted for publication.

Accepted Manuscripts are published online shortly after acceptance, before technical editing, formatting and proof reading. Using this free service, authors can make their results available to the community, in citable form, before we publish the edited article. We will replace this Accepted Manuscript with the edited and formatted Advance Article as soon as it is available.

You can find more information about Accepted Manuscripts in the [Information for Authors](#).

Please note that technical editing may introduce minor changes to the text and/or graphics, which may alter content. The journal's standard [Terms & Conditions](#) and the [Ethical guidelines](#) still apply. In no event shall the Royal Society of Chemistry be held responsible for any errors or omissions in this Accepted Manuscript or any consequences arising from the use of any information it contains.

An Efficient Heterodinuclear Ir(III)/Pt(II) Complex: Synthesis, Photophysics and Application in Light-Emitting Electrochemical Cells

View Article Online
DOI: 10.1039/C9TC02930C

Marsel Z. Shafikov,^{a,b*} Shi Tang,^c Christian Larsen,^c Michael Bodensteiner,^d Valery N. Kozhevnikov^{e*} and Ludvig Edman^{c*}

^a *Institut für Physikalische und Theoretische Chemie and ^d Zentrale Analytik Universität Regensburg, Universitätsstrasse 31, Regensburg, D-93053, Germany.*

^b *Ural Federal University, Mira 19, Ekaterinburg, 620002, Russia. E-mail: shafikoff@gmail.com*

^c *The Organic Photonics and Electronics Group, Department of Physics, Umeå University, SE-90187 Umeå, Sweden. E-mail: ludvig.edman@umu.se*

^e *Department of Applied Sciences, Northumbria University, Newcastle-Upon-Tyne, NE1 8ST, UK. E-mail: valery.kozhevnikov@northumbria.ac.uk*

Abstract

We report on the design, synthesis, characterization and successful application of a heterodinuclear Ir(III)/Pt(II) complex endowed with two 4,6-diphenylpyrimidine ligands and two acetylacetonate ligands, with one of the former being the rigid bridging unit between the two metal centers. The heterodinuclear complex exhibits red phosphorescence with a high quantum yield of $\Phi_{\text{PL}}=85\%$ and a short room-temperature decay time of $\tau=640$ ns in degassed toluene solution. The high efficiency of the spin-forbidden $T_1 \rightarrow S_0$ transition is demonstrated to originate in a strong spin-orbit coupling of the T_1 state with a manifold of excited singlet states, which contributes to the record-breaking zero-field splitting of the T_1 state of 240 cm^{-1} . The high-solubility and non-ionic hetero-dinuclear complex was employed as the emissive guest compound in host-guest light-emitting electrochemical cells, and such optimized devices delivered vibrant red emission ($\lambda_{\text{peak}} = 615\text{ nm}$) with a second-fast turn-on and a high external quantum efficiency of 2.7% at a luminance of 265 cd/m^2 .

1. Introduction

Transition metal complexes that incorporate more than one metal centre can offer efficient phosphorescence as well as a broad range of design opportunities.¹⁻⁸ The emission and processing properties of such multinuclear complexes are tuneable by the molecular design,^{4, 8-13} and, *e.g.*, the employment of a rigid conjugated bridging ligand between the metal centers over a flexible non-conjugated counterpart will result in a red-shifted emission, but at the expense of lowered solubility. A highly symmetric complex will further be prone to crystallization in the solid state, whereas a non-symmetric complex can allow for high solubility in common processing solvents and a facile solution-based fabrication of uniform thin films fit for low-cost device applications.

With such rich design properties at hand, it is not surprising that multinuclear complexes are gaining popularity as the emitting species in organic light-emitting diodes (OLEDs),^{1, 13-21} and also have contributed to an impressive device performance. For instance, Zhou and co-workers report on the successful application of Ir and Pt homodinuclear complexes as the emitter in OLEDs that exhibit a very high efficiency,^{13, 22} while others have demonstrated well-performing OLED devices based on homodinuclear and heterodinuclear complexes that emit with a broad variety of emission colors at high efficiency.²

The light-emitting electrochemical cell (LEC) features a number of distinct advantages over the OLED, notably the opportunity to employ a robust single-layer active material and air-stabile electrodes,²³⁻²⁹ which in turn render the LEC an ideal candidate for a low-cost³⁰ and low-energy solution-based³¹⁻³⁶

fabrication. However, only a few examples on the employment of multinuclear complexes in LEC devices exist in the scientific literature.³⁷⁻⁴³ Bideh and Shahroosvand³⁷ and Ju *et al.*³⁸ reported on ionic homodinuclear Ru complexes, which delivered strong emission with an external quantum efficiency (EQE) of 0.1-0.7% in LEC devices. Leprêtre and co-workers demonstrated non-ionic homodinuclear Ru complexes that exhibited orange emission in LECs with an EQE of 0.02 %, ³⁹ while Fernandez-Cestau *et al.* introduced novel heterotetranuclear Ir/Ag and Ir/Cu complexes equipped with alkynyl bridging ligands in LEC devices that delivered a peak luminance of ~20 cd/m².⁴⁰ Finally, Sessolo and co-workers recently reported on LECs based on an ionic homodinuclear Ir complex that featured an EQE of 0.83%.⁴² Accordingly, the use of multinuclear complexes in LEC is not yet as successful as in OLEDs and more comprehensive studies are needed in order to assess their full potential. At the same time, it is fundamental that the multinuclear complex is highly soluble in common solvents in order to be compatible with the solution-processing potential of LEC devices.

Here, we report on the design and synthesis of a non-symmetric and high-solubility non-ionic heterodinuclear complex, comprising Pt(II) and Ir(III) as the metal centers connected by a rigid 4,6-diphenylpyrimidine (dpp) bridging ligand and which is further equipped with a second dpp ligand and two acetylacetonate (acc) ancillary ligands. The heterodinuclear complex featured red emission with a high quantum yield of 85 % and a short phosphorescence decay time of 640 ns in toluene solution. A systematic photophysical investigation revealed that the high efficiency of the spin-forbidden T₁→S₀ transition originated in a strong spin-orbit coupling of the T₁ state with a manifold of excited singlet states which contributes to a record-breaking zero-field splitting of the T₁ state of 240 cm⁻¹. The non-ionic Pt/Ir heterodinuclear complex was employed as the guest emitter in host-guest LECs, which delivered vibrant red emission (λ_{peak} = 615 nm) with a fast turn-on time of 4 seconds and a high external quantum efficiency of 2.7 % at a significant luminance of 265 cd/m².

2. Experimental

Synthesis. All solvents and reagents were purchased from commercial suppliers and used without further purification unless otherwise noted. The synthesis of the starting complex **1** followed a published procedure.³ The complex **2** was prepared as follows. A mixture of complex **1** (750 mg, 0.77 mmol), K₂PtCl₄ (330 mg, 0.80 mmol) and acetic acid (130 cm³) was heated under reflux under nitrogen atmosphere for 2 days. The precipitated solid was filtered off and washed with methanol. The solid was transferred into a round-bottomed flask; ethoxyethanol (20 cm³) and sodium acetylacetonate (242 mg, 2.40 mmol) were added and the mixture was stirred under nitrogen atmosphere at 107°C for 14 h. Water (50 cm³) was added and the mixture was extracted with DCM (3 X 25 cm³). The organic layer was washed with water (50 cm³) and dried over anhydrous MgSO₄. The mixture was filtered and the filtrate was evaporated to dryness. The product was purified by column chromatography (silica gel, DCM). Yield 320 mg (33%).

NMR spectra were recorded on a JEOL ECS400FT Delta spectrometer (399.78 MHz for ¹H NMR, 100.53 MHz for ¹³C NMR). Chemical shifts are reported in parts per million (ppm) relative to a tetramethylsilane internal standard. Elemental microanalysis was carried out at University of Regensburg. High resolution mass spectroscopy (HRMS) was performed on a LTQ Orbitrap XL spectrometer at the EPSRC National Mass Spectrometry Service (University of Swansea).

NMR (400MHz, CDCl₃) δ 9.47 (s, 1H), 9.11 (s, 1H), 8.18 (d, *J* = 8.4 Hz, 2H), 8.09 (s, 1H), 7.83 (s, 1H), 7.75 (s, 1H), 7.60-7.66 (m, 5H), 7.26 (1H), 6.94 (d, *J* = 8.4 Hz, 2H), 6.56 (s, 1H), 6.42 (s, 1H), 2.03 (s, 3H), 1.91 (s, 3H), 1.86 (s, 3H), 1.84 (s, 3H), 1.42 (s, 18H), 1.08 (s, 9H), 1.05 (s, 9H).

Elemental analysis: calculated: C 54.79, H 5.31, N 4.41; measured: C 54.84, H 5.37, N 4.37.

HRMS: calculated (for MH⁺): C₅₈H₆₇N₄O₄¹⁹³Ir¹⁹⁵PtH 1272.4520; measured: 1272.4561.

X-ray diffraction. Red needle-shaped single crystals of complex **2** were obtained by slow convectional diffusion of methanol into a solution of **2** in dichloromethane. A representative 0.34×0.09×0.05 mm³

crystal was selected and mounted with mineral oil on a MITIGEN holder on a SuperNova diffractometer equipped with an Atlas CCD detector. The crystal was kept at $T = 123.01(10)$ K during data collection. The structure was solved with the ShelXT⁴⁴ structure solution program using the Intrinsic Phasing solution method and by using Olex2⁴⁵ as the graphical interface. The model was refined with version 2018/3 of ShelXL⁴⁴ using Least Squares minimization.

Optical spectroscopy. The photophysical measurements were performed on a solution of complex **2** in toluene. The UV-Vis absorption spectra were recorded with a Varian Cary 300 double beam spectrometer. The photoluminescence (PL) spectra were measured with a Horiba Jobin Yvon Fluorolog-3 steady-state fluorescence spectrometer, modified to allow for time-dependent measurements. The low-temperature measurements were performed with the sample mounted in a helium cryostat (Cryovac Konti Cryostat IT) in which the temperature can be varied between 1.7 and 300 K. The excitation source was a PicoBright PB-375 pulsed diode laser ($\lambda_{\text{exc}} = 378$ nm, pulse width 100 ps). The PL signal was detected with a cooled photomultiplier attached to a FAST ComTec multichannel scalar PCI card with a time resolution of 250 ps. The PL quantum yield was determined with a Hamamatsu C9920-02 system equipped with a Spectralon® integrating sphere.

Cyclic voltammetry. The cyclic voltammetry (CV) measurements were performed with a three-electrode setup controlled by an Autolab PGSTAT302 potentiostat/galvanostat (Eco Chemie). Complex **2** was dissolved in a dichloromethane/acetonitrile (1:10) mixed solvent at a solute concentration of ~1 g/l. A Au-coated glass plate was the working electrode, a Pt rod was the counter electrode, a Ag wire was the pseudo-reference electrode, and 0.1 M tetrabutylammonium hexafluorophosphate (TBAPF₆) in acetonitrile was the electrolyte solution. The pseudo-reference electrode was calibrated at the end of each experiment vs. the ferrocene/ferrocenium (Fc/Fc⁺) redox couple. The scan rate was 0.05 V/s. The reduction/oxidation onset potentials were defined as the intersection of the baseline with the tangent of the current at the half-peak height. The sample preparation and the CV scans were performed under N₂ atmosphere.

Device fabrication and characterization. Master solutions were prepared by separately dissolving complex **2**, poly(9-vinylcarbazole) (PVK), 1,3-bis[2-(4-tert-butylphenyl)-1,3,4-oxadiazole-5-yl]benzene (OXD-7), and tetrahexylammonium tetrafluoroborate (THABF₄) in chlorobenzene in a concentration of 20 g/l. The active-material inks were prepared by mixing the master solutions in the desired stoichiometries. A thin layer of poly(3,4-ethylenedioxythiophene)-poly(styrene sulfonate) (PEDOT-PSS, Clevios P VP Al 4083, Heraeus) was spin-coated onto carefully cleaned indium-tin-oxide (ITO) coated glass substrates (20 Ω /square, Thin Film Devices, US) at 4000 rpm for 60 s. The active-material ink was stirred on a magnetic hot plate at 343 K for at least 6 h and thereafter spin-coated onto the PEDOT-PSS layer at 2000 rpm for 60 s. The dry thickness of the PEDOT-PSS and active-material layers was 40 nm and 100 nm, respectively. A set of four Al electrodes was deposited on top of the active material by thermal evaporation at $p < 5 \times 10^{-4}$ Pa. The ITO electrode was biased as the positive anode during all measurements. The light-emission area, as defined by the cathode/anode overlap, was 0.85×0.15 cm². The LEC devices were characterized with a computer-controlled source-measure unit (Agilent U2722A) and a calibrated photodiode, equipped with an eye-response filter (S9219-01, Hamamatsu Photonics); the latter was connected to an embedded evaluation board (myRIO-1900, National Instruments) via a current-to-voltage amplifier. The electroluminescence (EL) spectrum was recorded with a calibrated fiber-optic spectrometer (USB2000+, Ocean Optics). All of the above procedures, except for the deposition of the PEDOT:PSS layer, were carried out in two interconnected N₂-filled glove boxes ([O₂] < 1 ppm, [H₂O] < 0.5 ppm).

3. Results and Discussion

3.1 Synthesis and XRD

View Article Online
DOI: 10.1039/C9TC02930C

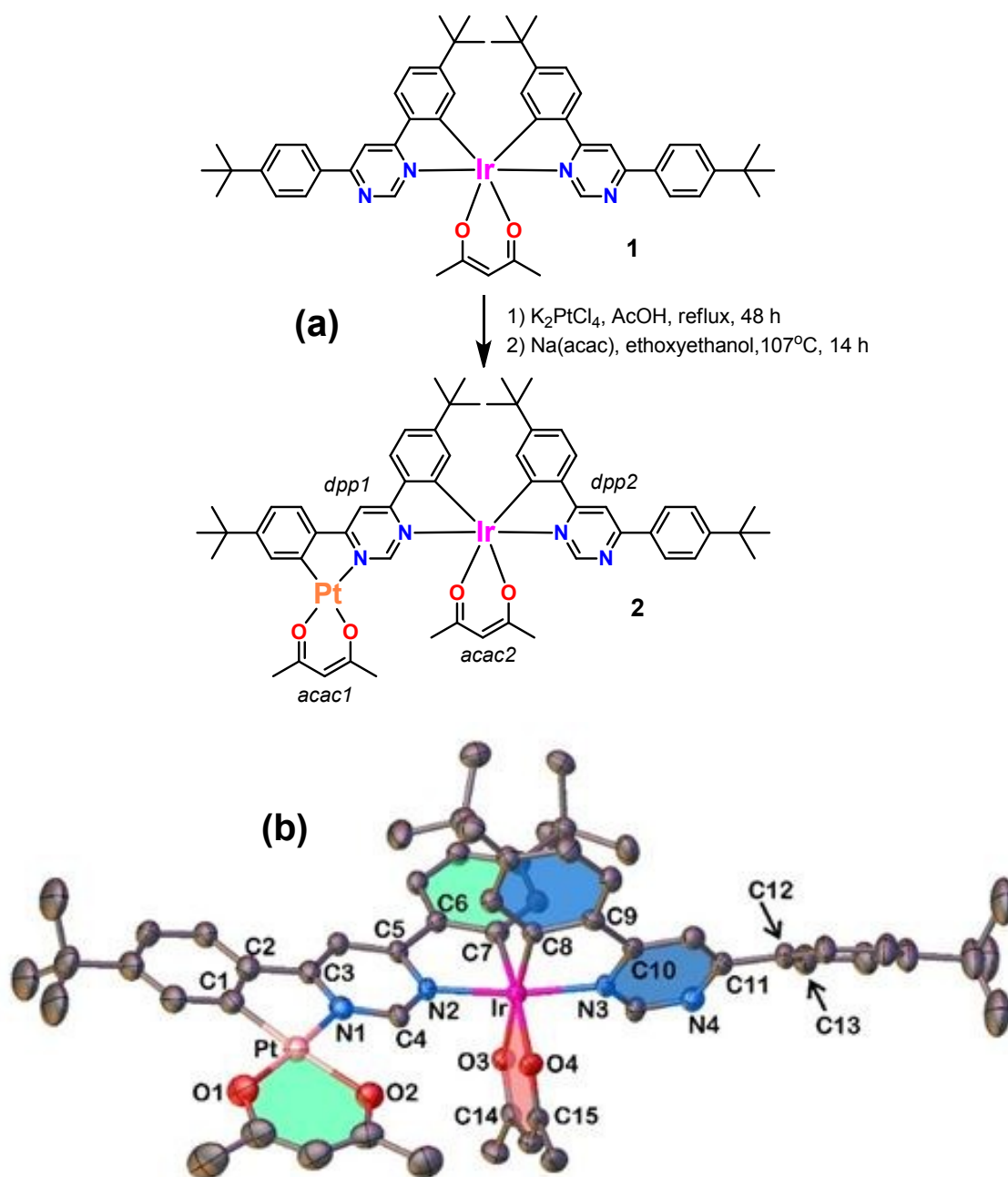


Figure 1. (a) The reaction scheme for the synthesis of complex 2. (b) The molecular structure of complex 2, as determined by XRD on a single crystal. The thermal ellipsoids are shown at 50% probability level and hydrogens are omitted for clarity.

The design goal was to realize a non-ionic multinuclear complex that features efficient phosphorescent emission in the red region, balanced and significant electrochemical doping capacity, and high solubility in common solvents fit for facile fabrication of uniform thin films. As such, the complex will be a strong candidate for the emitter in high-performance red-emitting LEC devices. For this end, we designed the mixed-metal heterodinuclear Ir(III)/Pt(II) complex 2 displayed in the lower part of Figure 1(a), with the Ir and Pt metal centers linked together by a rigid 4,6-diphenylpyridine (dpp1) bridging ligand, and with a second 4,6-diphenylpyridine (dpp2) ligand solely coordinated to the Ir center. A first

acetylacetonate (acac1) ligand was coordinated to the Pt center and a second acetylacetonate (acac2) ligand was coordinated to the Ir center. The inclusion of the *tert*-butyl end-capping units and the non-symmetric molecular character were expected to render the complex highly soluble in common organic solvents, and as such make it compatible with high-throughput solution-based fabrication.

The target complex **2** was prepared in a one-pot procedure by the reaction of complex **1** with one-molar equivalent of potassium tetrachloroplatinate in boiling acetic acid, as schematically outlined in Figure 1(a). The intermediate dichlorobridged complex was treated with sodium acetylacetonate, and the resulting complex **2** purified by column chromatography. The overall yield of the synthesis and purification procedures was 33 %, and the structure and purity were verified with ¹H NMR spectroscopy, high resolution mass-spectrometry and elemental analysis; see Experimental section for details.

The molecular structure of complex **2** in the crystalline state is displayed in Figure 1(b). It was obtained by X-ray diffraction (XRD) analysis of orthorhombic single crystals of complex **2**, grown by slow diffusion of methanol into a solution of complex **2** in dichloromethane. The corresponding coordination bond lengths and bond angles are reported in Table S2. We find that the Pt(II) metal center exhibits a square planar geometry with the acac1 ligand and the opposite dpp1 ligand (see Figure 1a for identification of the different ligands). More specifically, acac1 is only slightly twisted from dpp1, as quantified by the O1-Pt-C1-C2 and O2-Pt-N1-C3 torsion angles of 172.8° and 176.9°, respectively.

The Ir(III) metal center features an octahedral coordination geometry with the dpp2 ligand, the ancillary acac2 ligand and the dpp1 bridging ligand. The N2 atom of the dpp1 ligand and the N3 atom of the dpp2 ligand are in a *trans* configuration with a N2-Ir-N3 angle of 172.1°, while the C7 and C8 atoms are in a *cis* arrangement. The acac2 ligand has the O3 and O4 atoms in *trans* positions to C7 (dpp1) and to C8 (dpp2), respectively, with O3 being below and C8 above the plane of the dpp1 ligand (in the perspective of Figure 1b). The non-coordinated phenyl group of the dpp2 ligand is out of the coordination plane with a torsion angle N4-C11-C12-C13 of 28.4°. More details on the characterization procedures can be found in the Experimental section.

3.2 DFT, TD-DFT calculations and electronic structure analysis

The density functional theory (DFT) calculations were carried out on a model complex **2'**, with the *tert*-butyl substituents of complex **2** being truncated to methyl groups, to save computational time. The electronic structure was calculated with the Gaussian 09 code⁴⁶ at the M06⁴⁷/def2-SVP^{48, 49} level, while the time-dependent DFT (TD-DFT) calculations were performed at the M06L⁵⁰/def2-SVP level. To mimic the conditions of the experiments, the calculations were conducted with a conductor-like polarizable continuum model (C-PCM)⁵¹ applied with toluene as the solvent. The molecular geometry was optimized for the ground state (*S*₀) and the first excited triplet state (*T*₁) applying the "Tight" criteria.

Coordination center bond lengths and angles of the *S*₀ and *T*₁ state optimized geometries are presented in Table S2, while the corresponding calculated Cartesian coordinates are presented in Table S3. We find that the geometry of the *S*₀ ground state is in very good agreement with the XRD-measured solid-state geometry of complex **2**, as all of the coordination center bond lengths and almost all of the bond angles differ by less than 0.1 Å and 6°, respectively (see Table S2 for the comparison). The only difference is for the non-coordinated phenyl group of the dpp2 ligand, which is in the coordination plane of the ligand for **2'** in solution and out of the plane for **2** in the solid state (see Figure 1b). We attribute this difference to the more relaxed environment in the solution as compared to the crystalline solid state. The TD-DFT calculated absorption spectrum of **2'** is also in good agreement with the experimentally measured absorption spectrum of **2**, although the calculated spectrum is slightly red-shifted (see Figure S1). This validates the used theory level as correctly simulating the electronic structure of complex **2**. A summary of the TD-DFT-calculated optical transitions and a graphical presentation of the contour-plots of the corresponding orbitals are presented in Figure 2 and Tables S4-S9 in the SI.

For the emissive properties of complex **2**, the characteristics of the T_1 state are expected to be of highest relevance and our further discussions shall refer to the T_1 state geometry unless otherwise stated. The DFT data in Table S2 reveal that the geometry of the T_1 excited state primarily differs from the S_0 ground state at the Ir(III) coordination center. Specifically, the N2-Ir-O3-C14 and N2-Ir-O4-C15 torsion angles have decreased by more than 20° , which is indicative of a significant charge redistribution at the Ir(III) center between the ground state (S_0) and T_1 state. This is in line with the charge transfer character of the T_1 state, as suggested by the TD-DFT calculations and discussed further below.

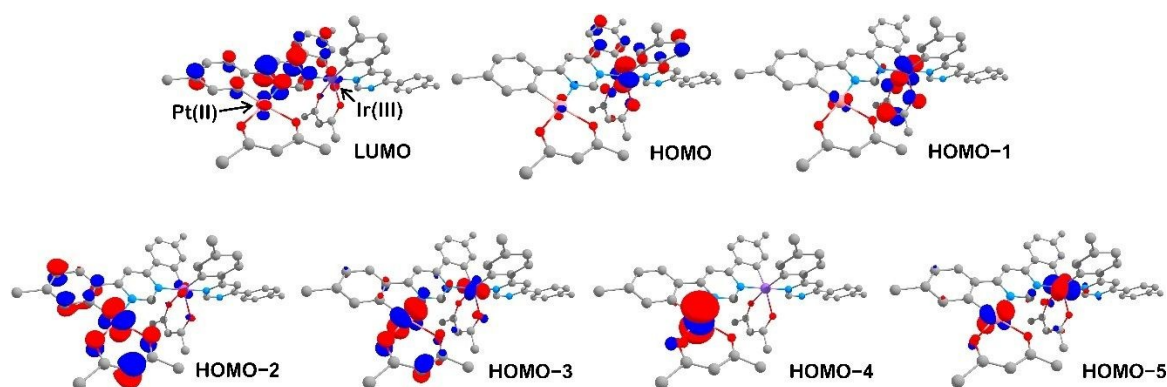


Figure 2. The iso-surface contour plots of the orbitals of model complex **2'** (T_1 state geometry) contributing to formation of state T_1 (HOMO and LUMO). Also shown are iso-surface contour-plots of occupied orbitals that contribute to excited singlet states and afford them for direct SOC with state T_1 (HOMO- n , $n>0$). The contour plots are reproduced at iso-value=0.05. Hydrogens are omitted for clarity.

The electronic $T_1 \rightarrow S_0$ transition is formally forbidden by the spin-selection rule $\Delta S=0$. This rule can however be relaxed by spin-orbit coupling (SOC) of state T_1 state with excited singlet states.⁵² This effect is often prominent in complexes comprising heavy transition metals with a large spin-orbit coupling constants, such as Pt(II) ($\zeta_t=4481 \text{ cm}^{-1}$) and Ir(III) ($\zeta_t=3909 \text{ cm}^{-1}$),⁵³ and these complexes can therefore be highly emissive (or phosphorescent) via the $T_1 \rightarrow S_0$ transition.⁵⁴

Two states can have effective direct SOC only if three conditions are met: (i) the two states should be in a close energetic proximity.⁵⁵ (ii) The same natural transition orbital (NTO, hole or electron) of the two states should be contributed by the same heavy atom at which the unpaired electron's spin can flip. This requirement is dictated by the one-electron and short-range character of the SOC effect. (iii) The heavy atom should contribute to the states with different orbitals (different d-orbitals in the case of Ir atom) to conserve the total momentum (orbital+spin) of the electron when its spin flips.^{56, 57} The latter is also known as the El-Sayed rule.

According to TD-DFT calculations, state T_1 has HOMO \rightarrow LUMO origin, where HOMO is strongly contributed by an Ir 5d orbital (d_i), whereas the LUMO is largely represented by a π^* orbital localized on the dpp1 ligand (Figure 2). Thus, according to these data the triplet state T_1 can be assigned a Metal-to-Ligand Charge Transfer character (${}^3\text{MLCT}^{\text{Ir(III)}}$) involving the Ir(III) center that can also be denoted as a ${}^3d_i\pi^*$ excited state. The requirements for effective SOC, as given above, are that a state of ${}^3d_i\pi^*$ character (T_1) can effectively couple only with singlet states of ${}^1d_j\pi^*$ character for which $d_i \neq d_j$ (but d_i and d_j belong to the same atom) and $\pi^* = \pi'^*$ is true. Accordingly, state T_1 of complex **2** can couple with close in energy singlet states contributed by a HOMO- $n \rightarrow$ LUMO transition where HOMO- n ($n>0$) is an occupied orbital contributed by the Ir atom and different from HOMO (for $d_i \neq d_j$). Analysis of the TD-DFT data shows that within 0.5 eV energy gap state T_1 can couple via SOC with state S_1 (has 3% contribution from HOMO-1 \rightarrow LUMO transition) and state S_3 (has 92% contribution from HOMO-1 \rightarrow LUMO transition). State S_2 contributed solely by HOMO \rightarrow LUMO+1 transition does not

fulfill $d_i \neq d_j$ and $\pi^* = \pi'^*$ requirements to have direct SOC with state T_1 . According to the electronic origin of state S_3 its SOC with state T_1 at the Ir center is expected to be particularly strong, which, due to a comparatively high oscillator strength ($f(S_0 \rightarrow S_3) = 0.0707$), would well contribute to the phosphorescence rate ($k_r(T_1 \rightarrow S_0)$). In the range 0.5 – 1 eV above state T_1 singlet states S_4 - S_8 and S_{10} are contributed by transitions HOMO- $n \rightarrow$ LUMO with $n \geq 2$ strongly involving Pt atom (Figure 2 and Table S5 and S7 in the SI). Since state T_1 is of HOMO \rightarrow LUMO origin and HOMO is contributed mildly by the Pt atom (Figure 2, Table S7 in the SI), these higher lying singlets can have some SOC with state T_1 also at the Pt(II) center. Thus, the analysis of the TD-DFT data predicts that state T_1 has significant singlet admixtures via primary SOC at the Ir center and some less profound but still contributing SOC at the Pt center. Hence, a comparatively high phosphorescence rate can be expected for complex **2**.

3.3 Optical spectroscopy

The absorption and photoluminescence (PL) spectra of complex **2** in toluene at room temperature are shown in Figure 3(a), and key numerical data are summarized in Table 1. The absorption spectrum features three distinct regions, which according to literature and TD-DFT data are interpreted as follows: (i) the low-intensity bands ($\epsilon \approx 10000 \text{ M}^{-1}\text{cm}^{-1}$) at 500-600 nm represent charge-transfer transitions from the Ir(III) center to the dpp1 and dpp2 ligands^{10, 58, 59} and are assigned to $^1\text{MLCT}^{\text{Ir(III)}}$ states; (ii) the medium-intensity bands ($\epsilon \approx 20000 \text{ M}^{-1}\text{cm}^{-1}$) at 380-500 nm originate in transitions from either solely the Pt(II) center or a combination of the Pt(II) and Ir(III) centers to the dpp1 and dpp2 ligands, which are accordingly assigned to states of either $^1\text{MLCT}^{\text{Pt(II)}}$ or $^1\text{MLCT}^{\text{Pt(II)/Ir(III)}}$ character;^{9, 10, 60} (iii) the high-intensity bands with the maxima at 326 nm are assigned to states of $\pi\pi^*$ character within the [dpp1-Pt-acac1] moiety and the dpp2 ligand with minor contribution from a ligand-to-ligand charge-transfer ($^1\text{LLCT}$) transition (See Tables S4 and S6 in the SI).

The PL spectrum of complex **2** (in toluene solution at room temperature) appears in the red spectral region, with the maximum at $\lambda_{\text{max}} = 615 \text{ nm}$. This represents a slight red-shift in comparison to the starting mononuclear Ir complex **1** that emits at $\lambda_{\text{max}} = 585 \text{ nm}$. The red-shift is rationalized as being the result of the extension of dpp1 ligand's π -conjugated system to the Pt(II) ion and the acac1 ligand, which decreases the HOMO–LUMO energy gap. We also note that the PL spectrum is broad and unstructured, which is characteristic for the emission from a charge-transfer state^{9-11, 54, 60-63} due to a strong Franck-Condon coupling of the T_1 state and the ground state. We finally note that a corresponding mononuclear Pt complex is reported to emit at $\lambda_{\text{max}} = 513 \text{ nm}$ (in dichloromethane at room temperature).³ The measured PL quantum yield of **2** in degassed toluene at room temperature is very high at $\Phi_{\text{PL}} = 85\%$ with a decay time of only $\tau(300 \text{ K}) = 640 \text{ ns}$. These values reveal an outstanding radiative rate (calculated as $k_r = \Phi_{\text{PL}}/\tau$) of $k_r = 1.33 \cdot 10^6 \text{ s}^{-1}$ that is an order of magnitude higher than of the fastest Pt(II) complexes^{64, 65} and notably higher than most other Ir(III) complexes.^{54, 63, 66} This behavior is in line with the TD-DFT results, and shows the dominant role of the Ir(III) center in the properties of the T_1 state and the PL characteristics of complex **2**. A radiative rate of similar magnitude has only been reported for a few Ir(III) complexes, primarily of di-nuclear design.^{10, 11, 60, 67} It is noted that high efficiency phosphorescence is particularly valuable for a red emitter, since the Einstein's constant of spontaneous emission is inversely proportional to the cube of emission wavelength ($1/\lambda^3$), whereas the non-radiative rate increases exponentially with decreasing energy gap between the emitting state and the ground state, as dictated by the energy gap law.⁶⁶

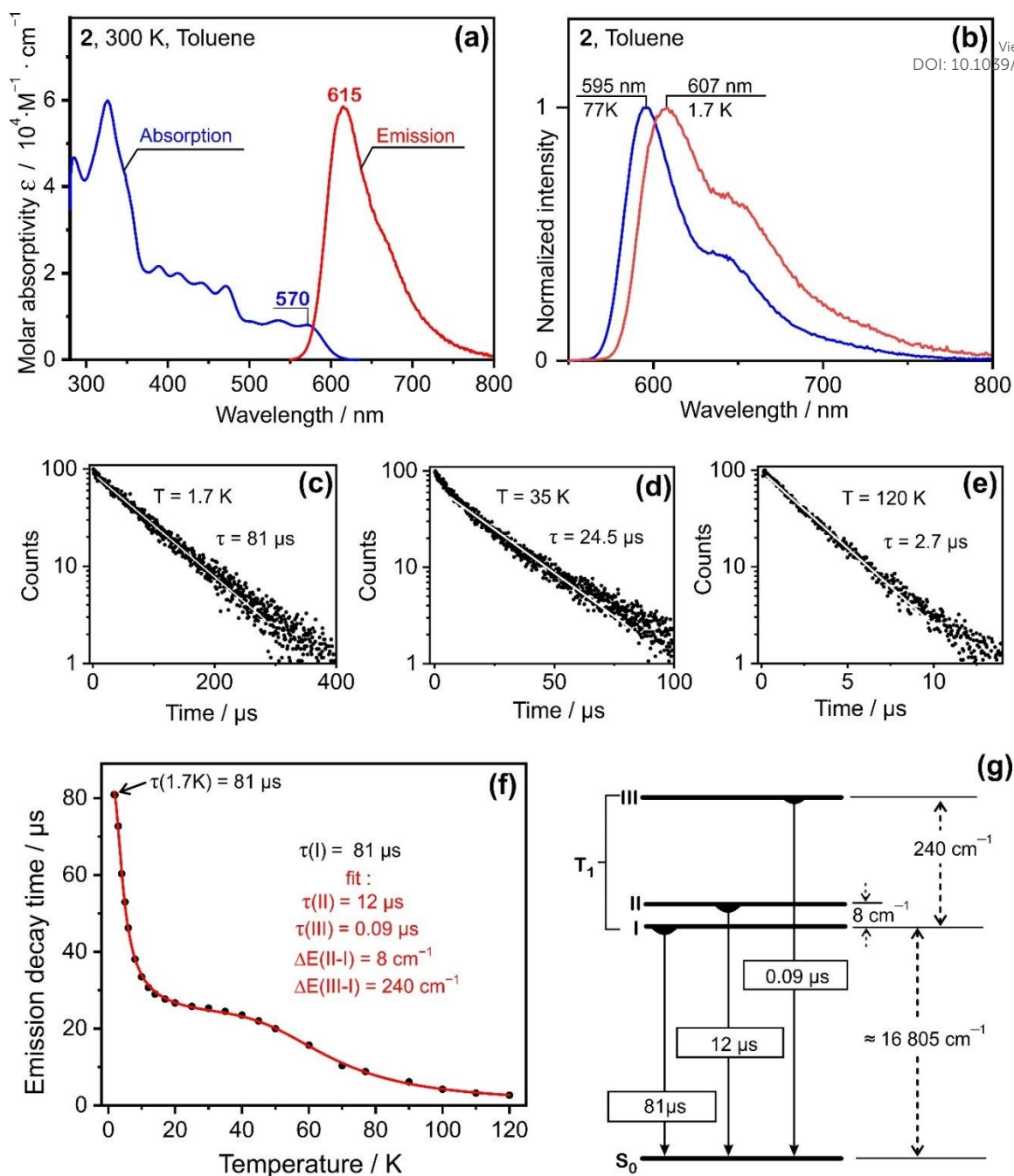


Figure 3. (a) The absorption and photoluminescence (PL) spectra of complex **2** in toluene ($c \approx 10^{-5} \text{ M}$) at room temperature. (b) The PL spectra of **2** in toluene at 1.7 K (red trace) and 77 K (blue trace). (c-e) The PL decay curves of **2** in toluene at different temperatures, as specified in the upper insets. (f) A summary of the measured PL decay times as a function of temperature (black dots), and the best fit of Eq. 1 to the experimental values (red line). The concentration of **2** is $c \approx 10^{-5} \text{ M}$, and the PL excitation wavelength in (a-f) is 378 nm. (g) A simplified energy-level diagram depicting the three zero-field-split T_1 states and the S_0 ground state, and the corresponding $T_1 \rightarrow S_0$ PL decay times. Note that the diagram is not to scale.

Table 1. A summary of key photophysical properties of complex **2** in toluene solution ($c \approx 10^{-5}$ M).

View Article Online
DOI: 10.1039/C9TC02930C

Absorption	570 (8043), 535 (9068), 503 (8800), 471 (17036), 441 (17783) 412 (20025), 389 (21635), 326 (59917), 285 (46600)
λ_{\max}/nm	
$(\epsilon / \text{M}^{-1}\text{cm}^{-1})$	
Photoluminescence	
300 K*	
λ_{\max}/nm	615
Φ_{PL}	0.85
$\tau / \mu\text{s}$	0.64
$k_r / 10^6 \text{ s}^{-1}$	1.33
$k_{\text{nr}} / 10^6 \text{ s}^{-1}$	0.23
77 K	
λ_{\max}/nm	595, 645
Φ_{PL}	0.80
$\tau / \mu\text{s}$	8.80

*The reported data are obtained for a degassed solution.

The measured fast phosphorescence of complex **2** implies a strong mixing of the T_1 state with the excited singlet states via SOC, as was predicted by the TD-DFT calculations. The strength of T_1 state SOC with singlets states can be quantified through the zero-field splitting (ZFS) of T_1 sub-states I, II, and III and their individual decay times.⁶⁸⁻⁷⁰ Since the three T_1 sub-states are split in energy by the SOC to other states (triplet and singlet), population of an individual T_1 sub-state depends on temperature. This affects the average (measured) $T_1 \rightarrow S_0$ emission decay time that becomes prominent at low temperatures where thermal population of the higher T_1 sub-states II and III is not so efficient. Hence PL decay time values measured as a function of temperature can yield information on the ZFS and individual decay times of the T_1 sub-states I, II, III.^{57, 64, 71, 72}

At temperature $T = 1.7$ K the PL decay time is $\tau(1.7\text{K}) = 81 \mu\text{s}$ (Figure 3c), and we assign this value to the transition from the lowest T_1 sub-state I to the ground state, $I \rightarrow S_0$. With increase of temperature the PL decay time is observed to decrease strongly, which is due to the thermal population of the higher triplet sub-state II and the opening of an additional transition channel $II \rightarrow S_0$. In the temperature range of $20 \leq T \leq 40$ K, the PL decay time forms a quasi-plateau, with the average decay time of the sub-states I and II of $\tau(I/II) \approx 25 \mu\text{s}$ measured at $T=35$ K (Figure 3d). A further increase of the temperature is accompanied by a drop of the PL decay time by an order of magnitude to $\tau(120\text{K}) = 2.7 \mu\text{s}$ (Figure 3e), which is due to the thermal population of the highest triplet sub-state III and the opening of the $III \rightarrow S_0$ decay channel. This gradual population of higher and faster emitting triplet sub-states II and III with increasing temperature is also traced in a notable blue-shift of the PL spectrum from $T=1.7$ K ($\lambda_{\text{em}}=607$ nm) to $T=77$ K ($\lambda_{\text{em}} = 595$ nm) shown in Figure 3(b).

An analysis of the PL decay time values as a function of temperature with the Boltzmann type equation (1)⁷³⁻⁷⁵ reveals photophysically important characteristics of the T_1 state.

$$\tau(T) = \frac{1 + \exp\left(\frac{-\Delta E(\text{II-I})}{k_B T}\right) + \exp\left(\frac{-\Delta E(\text{III-I})}{k_B T}\right)}{\frac{1}{\tau(\text{I})} + \frac{1}{\tau(\text{II})} \exp\left(\frac{-\Delta E(\text{II-I})}{k_B T}\right) + \frac{1}{\tau(\text{III})} \exp\left(\frac{-\Delta E(\text{III-I})}{k_B T}\right)} \quad (1)$$

View Article Online
DOI: 10.1039/C9TC02930C

Here $\tau(\text{I})$, $\tau(\text{II})$, $\tau(\text{III})$ are the decay times of triplet sub-states I, II and III, respectively; $\Delta E(\text{II-I})$ and $\Delta E(\text{III-I})$ are the energy gaps between sub-states II and I, and sub-states III and I, respectively; T is the temperature; and k_B is the Boltzmann constant. Equation (1) was fitted to the emission decay time data points with the fixed parameter $\tau(\text{I}) = 81 \mu\text{s}$ which is a value obtained experimentally at $T=1.7 \text{ K}$. The best fit, shown in Figure 3f, derives sub-state II and III individual decay times as being of $\tau(\text{II}) = 12 \mu\text{s}$ and $\tau(\text{III}) = 0.09 \mu\text{s}$, respectively, and energy gap values $\Delta E(\text{II-I}) = 8 \text{ cm}^{-1}$ and $\Delta E(\text{III-I}) = 240 \text{ cm}^{-1}$. The derived T_1 state ZFS value of 240 cm^{-1} is the largest reported so far for an Ir(III) complex and that evidences particularly strong SOC of state T_1 with other states. The obtained individual decay times are comparatively short, especially for sub-state III. The decay time value as short as $\tau(\text{III}) = 0.09 \mu\text{s}$ shows a particularly large singlet admixture to sub-state III, so that in respect to relaxation to the ground state it behaves almost like a singlet state. Therefore, the record breaking ZFS size of state T_1 of complex **2** has to be strongly contributed by SOC to the singlet states. For comparison, the previous record T_1 state ZFS of 170 cm^{-1} was reported for fac-Ir(ppy)₃ (ppy=2-phenylpyridine) with individual T_1 sub-state decay times of $\tau(\text{I})=116 \mu\text{s}$, $\tau(\text{II})=6.4 \mu\text{s}$ and $\tau(\text{III})= 0.2 \mu\text{s}$.⁷²

A comparatively strong T_1 state SOC with the singlet states for complex **2** was foreseen on the basis of TD-DFT data above in section 3.2, which predicted effective SOC channels at the Ir(III) center and some less significant but contributing SOC at the Pt(II) center. Therefore, it can be concluded that the outstanding emissive properties of state T_1 of complex **2** is the benefit of the di-nuclear molecular design. This conclusion is further supported by the notably higher phosphorescence rate of complex **2** compared to the mono-nuclear Ir(III) complex **1** (Scheme 1) that was reported earlier.⁹

3.4 Device development and characterization

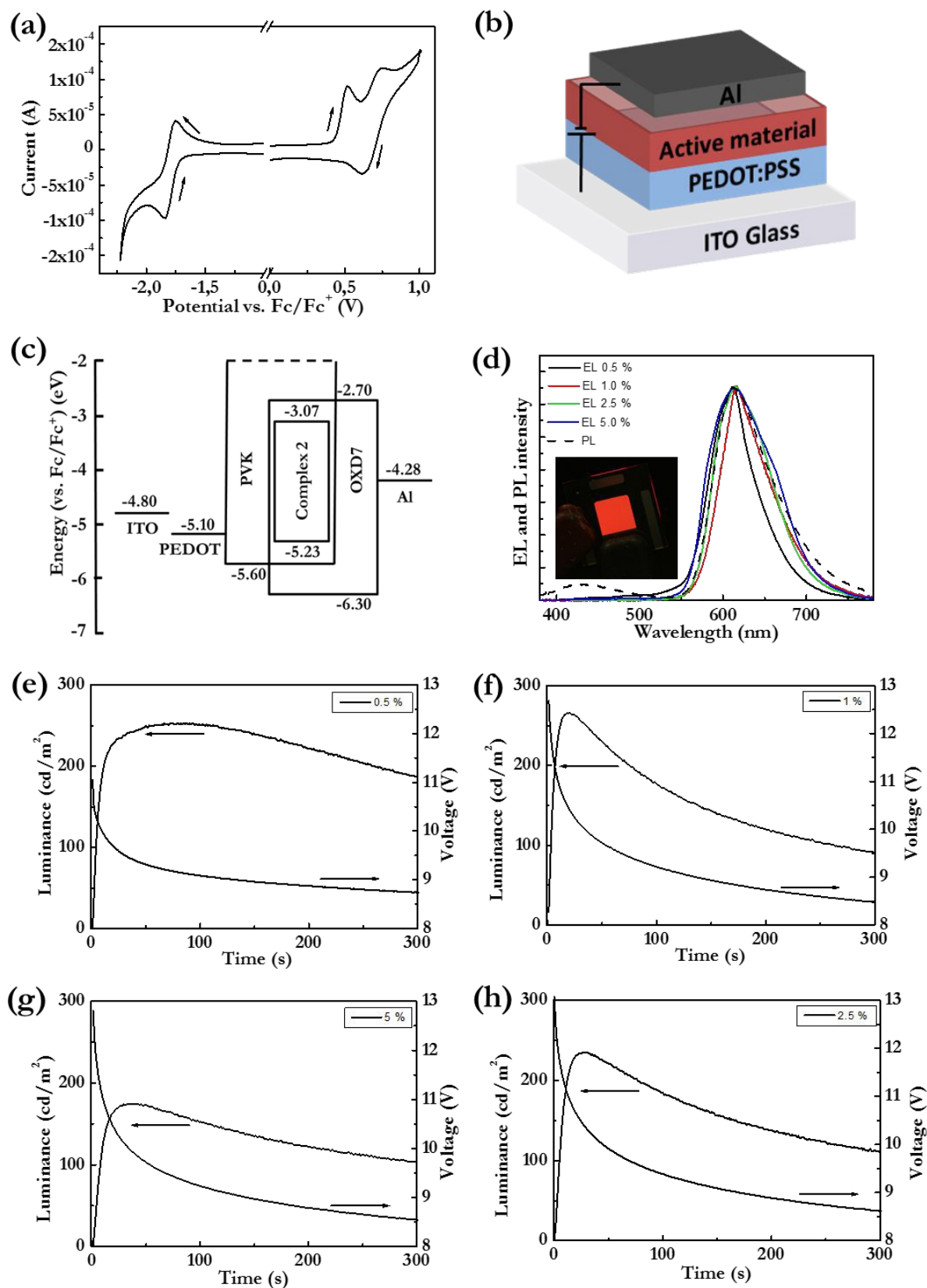


Figure 4. (a) Cyclic voltammetry traces of complex 2 in dichloromethane:acetonitrile (1:10) solution at a concentration of ~ 1 g/l. The scan rate was 0.05 V/s. (b) A schematic of the LEC device structure. (c)

The energy structure of the constituents in the LEC devices. (d) The PL spectrum of the LEC active material with 1 mass% guest concentration (dashed line), and the steady-state EL spectrum of LEC devices with the guest concentration identified in the upper left inset. A photograph depicting the $8 \times 8 \text{ mm}^2$ light-emission area of a LEC with 1 mass% guest concentration is included as the lower left inset. (e-h) The LEC transients of the LEC devices with the guest concentration defined in the insets.

Table 2. The PLQY of the active-material film and the LEC device performance as a function of guest concentration.

Host:Guest (mass ratio)	PLQY ¹ (%)	EL peak ² (nm)	CIE (x,y)	Turn-on time (s) ³	Peak luminance (cd/m ²)	Current efficacy (cd/A)	Power efficacy (lm/W)	EQE (%)
100:0.5	40.8	612	0.60, 0.38	4	252	3.3	1.1	2.6
100:1	41.7	615	0.62, 0.35	4	265	3.4	1.0	2.7
100:2.5	46.6	613	0.62, 0.36	5	235	3.0	0.9	2.4
100:5	52.7	614	0.62, 0.38	8	174	2.3	0.7	1.8

¹ In thin film. ² At steady-state. ³ Turn-on time to 100 cd/m²

With the promising basic photophysical properties of complex **2** established, we turn to the investigation of its merit for the electroactive and emissive compound in an LEC device. It is paramount that the electroactive compound in an LEC can be electrochemically p-type doped (oxidized) at the anode and n-type doped (reduced) at the cathode, so that a light-emitting p-n junction can form in the center of the active material when the two doping regions meet.^{24, 76} With the p-n junction doping structure in place, the holes can be efficiently injected into, and transported through, the p-type region, while electrons are injected into and transported through the n-type region; the holes and electrons meet and recombine into excitons at the p-n junction, and these excitons can decay by the emission of photons.⁷⁷

A convenient method of investigating whether a compound can be electrochemically doped is cyclic voltammetry (CV), and Figure 4(a) presents CV traces recorded on complex **2**. The CV data demonstrate that complex **2** can be both oxidized and reduced by electrochemistry, and that the oxidation and reduction reactions are relatively balanced and reversible. It is thus established that complex **2** feature the prerequisites for electrochemical p-type and n-type doping. We further use the CV data to estimate the energetic positions of the HOMO and LUMO levels of complex **2** with respect to the vacuum level (VL), using the following equation:

$$E_{\text{VL}} = - (4.8 \text{ eV} + eV_{\text{Fc/Fc}^+}) \quad (2)$$

where e is the elementary charge and $V_{\text{Fc/Fc}^+}$ is the measured onset potential for the redox reaction with respect to the Fc/Fc⁺ reference electrode. We find that the HOMO level of complex **2** is positioned at -5.23 eV below the VL, and the LUMO level at -3.07 eV.

It is further fundamental to include mobile ions (an electrolyte) into the active material of an LEC device, since it is the redistribution of these mobile ions that allow for the electrochemical doping to take place. For this task, we have selected the ionic liquid THABF₄, because it features a very broad electrochemical stability window, which renders it robust towards undesired electrochemical side reactions.⁷⁸ Triplet-emitting compounds, such as complex **2**, are commonly dispersed in a host matrix in electroluminescent devices in order to lower the risk for detrimental triplet-triplet quenching reactions.⁷⁹ We have employed a blend of PVK and OXD-7 in a 1:1 mass ratio for the host matrix, since this host blend features balanced hole and electron mobility⁸⁰ as well as balanced p-type and n-type doping capacity⁸¹.

A further criterion for efficient LEC operation is that the solid active material should feature a high photoluminescence quantum yield (Φ_{PL}), and we measure values for Φ_{PL} of 41-53 % for the optimized

(PVK+OXD-7+Complex **2**+THABF₄) active-material thin film depending on the concentration of the complex **2** guest; see Table 2 for a summary. As these values are both high and rather close to the value of 85 % for complex **2** in dilute solution, we draw the conclusion that the complex **2** guest is well dispersed in the active material, and that triplet-triplet quenching reactions are efficiently suppressed. Further support for a well-dispersed guest in the active material is provided by the strong resemblance between the PL spectrum of complex **2** in dilute solution (Fig. 3b, red trace) and the PL spectrum of the active material (Fig. 4d, dashed line). The minor PL peak at ~430 nm from the active material is attributed to remnant emission from the blend host.

The LEC devices were fabricated with the active material sandwiched between an ITO/PEDOT:PSS anode and an Al cathode. Figure 4(b) presents a schematic of the device structure while Figure 4(c) displays the energetics of the device constituents. We call specific attention to that the electron/hole trap levels, defined as the energetic difference between the lowest-LUMO/highest-HOMO of the blend host and the LUMO/HOMO of the guest, are well balanced at -0.37 eV, since such a balance has been demonstrated to be a prerequisite for high-efficiency operation of strongly luminescent host-guest LECs.⁸¹

The LEC devices were driven by a constant current density of $j = 7.7 \text{ mA/cm}^2$, and Figure 4(d) presents the steady-state EL spectrum for four different guest concentrations ranging from 0.5 to 5 mass%, as identified in the inset. The EL spectrum is centered at 612-615 nm (see Table 2) and essentially invariant to the guest concentration. In consideration of that the host blend emits at ~430 nm, it is clear that the host-to-guest energy transfer is complete in the LEC devices even at a low guest concentration of 0.5 mass%. We have also recorded the EL spectrum for the 1 mass% guest concentration device at different drive voltages, and Figure S2 reveals that the EL spectrum as well as the color coordinates (0.62, 0.35) are essentially invariant to the driving conditions. A photograph of the red emission from a $8 \times 8 \text{ mm}^2$ LEC with 1 mass% guest concentration is presented in the lower left inset of Figure 4(d).

Figures 4(e-h) show the initial operation of four representative LEC devices, distinguished by the concentration of guest in the active material. All four devices exhibit the two characteristic initial LEC transients at constant-current operation: a decreasing voltage and an increasing luminance. The former is essentially attributed to the doping reactions that render the active material more conductive, while the latter can be assigned to the perfectly balanced recombination of electrons and holes that follow from p-n junction doping formation.⁸²

The optimized LEC devices exhibit a fast turn on of a few seconds (to a significant luminance of 100 cd/m^2), which allows us to conclude that the active-material morphology allows for fast transport of the bulky THA cations and BF₄ anions.⁸³ We speculate that the non-symmetric and bulky structure of complex **2** has contributed to a desired formation of free volume in the active material for facile ion transport. We have also performed an atomic force microscopy study, which showed that the active material features a desirable smooth surface morphology with a very minor root-mean-square surface roughness of <1 nm (Figure S3). We further observe that the peak in luminance significantly precedes the minimum in voltage, which implies that the maximum in doping (at the minimum in voltage) is concomitant with significant exciton-quenching reactions.⁸⁴ We also note that the initial voltage increases somewhat with increasing guest concentration, but that the steady-state voltage appears to be relatively independent on the guest concentration.

Importantly, all four LEC devices exhibit high efficiency at significant luminance, with the best combined performance -- a luminance of 265 cd/m^2 delivered at an EQE of 2.7 % -- being attained from the host-guest LEC with a complex **2** guest concentration of 1 mass% (see Figure 4f). This achievement represents a significant improvement over the efficiency state-of-the-art for multinuclear-complex based LECs, since it is the first time such a device breaks the 1% barrier for the EQE. We also note that the overall best performance from red-emitting LECs based on any of the incumbent emitters, in the form of a mononuclear ionic transition metal complex or a conjugated polymer, is an EQE of 9.51 % measured at a luminance of 154 cd/m^2 ,²³ and that the herein introduced

device thereby introduces the dinuclear complex as a serious contender for the emitting species in efficient LEC devices.

View Article Online
DOI: 10.1039/C9TC02930C

Conclusions

We report on the successful design and synthesis of a heterodinuclear Ir(III)/Pt(II) complex, which exhibits efficient red phosphorescence, balanced electrochemical p-type and n-type doping capacity and high solubility in common organic solvents such as toluene. Through systematic photophysical measurements and calculations, we pinpoint that the efficient phosphorescence stems from the T_1 state that is strongly perturbed by spin-orbit coupling with a manifold of excited singlet states. This perturbation is manifested in a notably high zero-field splitting for the T_1 state of 240 cm^{-1} . We incorporate the non-ionic and high-solubility heterodinuclear complex as the guest emitter in host-guest light-emitting electrochemical cells, and attain vibrant red emission with a second-fast turn-on and a high external quantum efficiency of 2.7%. We attribute the promising performance of the red-emitting LEC to the high photoluminescence quantum yield of the active material of >40%, the capacity for efficient triplet emission by the heterodinuclear complex, the balanced electrochemical doping capacity of the electroactive compounds, and the similar sized electron and hole traps. Importantly, the herein demonstrated competitive performance of multinuclear LEC devices implies that this group of novel emitters could be developed into a serious alternative contender to the incumbent mononuclear complexes^{25, 85, 86} and conjugated polymers^{24, 82, 87}.

Accession Codes

CCDC 1901014 contains the supplementary crystallographic data for this paper. The data can be obtained free of charge via www.ccdc.cam.ac.uk/data_request/cif or by e-mailing data_request@ccdc.cam.ac.uk or by contacting The Cambridge Crystallographic Data Centre, 12 Union Road, Cambridge

CB2 1EZ, U.K.; fax: +44 1223 336033

ORCID

Marsel Z. Shafikov: 0000-0003-0495-0364

Christian Larsen: 0000-0002-2480-3786

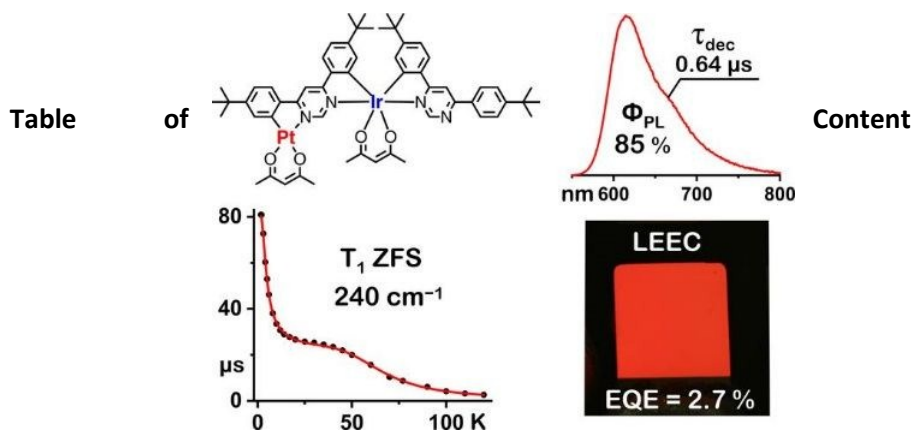
Michael Bodensteiner: 0000-0002-1850-5192

Valery N. Kozhevnikov: 0000-0001-7032-8886

Ludvig Edman: 0000-0003-2495-7037

Acknowledgements

M.Z.S. thanks the German Research Foundation (DFG) for financial support (Project No 389797483) and Professor Duncan Bruce and the University of York, U.K., for use of computational facilities. L.E. S.T. and C.L. acknowledge financial support from the Swedish Foundation for Strategic Research, the Swedish Research Council, the Swedish Energy Agency, Stiftelsen Olle Engkvist Byggmästare, and Bertil & Britt Svenssons stiftelse för belysningsteknik.



A novel heterodinuclear Ir(III)/Pt(II) complex delivers vibrant red phosphorescence with high efficiency in a light-emitting electrochemical cell.

References

View Article Online
DOI: 10.1039/C9TC02930C

1. E. V. Puttock, M. T. Walden and J. A. G. Williams, *Coordination Chemistry Reviews*, 2018, **367**, 127-162.
2. Q. C. Zhang, H. Xiao, X. Zhang, L. J. Xu and Z. N. Chen, *Coordination Chemistry Reviews*, 2019, **378**, 121-133.
3. V. N. Kozhevnikov, M. C. Durrant and J. A. G. Williams, *Inorganic Chemistry*, 2011, **50**, 6304-6313.
4. S. Culham, P.-H. Lanoë, V. L. Whittle, M. C. Durrant, J. A. G. Williams and V. N. Kozhevnikov, *Inorganic Chemistry*, 2013, **52**, 10992-11003.
5. Y. L. Zhao, Y. M. Li, T. Z. Yu, X. Y. Li, X. X. Liu, Y. J. Wang and H. Zhang, *J. Organomet. Chem.*, 2018, **877**, 51-58.
6. M. Z. Shafikov, R. Daniels, P. Pander, F. B. Dias, J. A. G. Williams and V. N. Kozhevnikov, *ACS Applied Materials & Interfaces*, 2019, **11**, 8182-8193.
7. R. E. Daniels, S. Culham, M. Hunter, M. C. Durrant, M. R. Probert, W. Clegg, J. A. G. Williams and V. N. Kozhevnikov, *Dalton Transactions*, 2016, **45**, 6949-6962.
8. G. Turnbull, J. A. G. Williams and V. N. Kozhevnikov, *Chemical Communications*, 2017, **53**, 2729-2732.
9. V. N. Kozhevnikov, M. C. Durrant and J. A. G. Williams, *Inorg. Chem.*, 2011, **50**, 6304-6313.
10. P.-H. Lanoë, C. M. Tong, R. W. Harrington, M. R. Probert, W. Clegg, J. A. G. Williams and V. N. Kozhevnikov, *Chem. Commun.*, 2014, **50**, 6831-6834.
11. R. E. Daniels, S. Culham, M. Hunter, M. C. Durrant, M. R. Probert, W. Clegg, J. A. Williams and V. N. Kozhevnikov, *Dalton Trans.*, 2016, **45**, 6949-6962.
12. R. E. Daniels, L. K. McKenzie, J. R. Shewring, J. A. Weinstein, V. Kozhevnikov and H. E. Bryant, *RSC Advances*, 2018, **8**, 9670-9676.
13. X. Yang, Z. Feng, J. Zhao, J.-S. Dang, B. Liu, K. Zhang and G. Zhou, *ACS Applied Materials & Interfaces*, 2016, **8**, 33874-33887.
14. Q.-C. Zhang, H. Xiao, X. Zhang, L.-J. Xu and Z.-N. Chen, *Coordination Chemistry Reviews*, 2019, **378**, 121-133.
15. G. Li, D. G. Congrave, D. Zhu, Z. Su and M. R. Bryce, *Polyhedron*, 2018, **140**, 146-157.
16. X. Yang, X. Xu, J.-s. Dang, G. Zhou, C.-L. Ho and W.-Y. Wong, *Inorganic Chemistry*, 2016, **55**, 1720-1727.
17. S. Yang, F. Meng, X. Wu, Z. Yin, X. Liu, C. You, Y. Wang, S. Su and W. Zhu, *Journal of Materials Chemistry C*, 2018, **6**, 5769-5777.
18. Z. Hao, F. Meng, P. Wang, Y. Wang, H. Tan, Y. Pei, S. Su and Y. Liu, *Dalton Transactions*, 2017, **46**, 16257-16268.
19. Y. Zheng, A. S. Batsanov, M. A. Fox, H. A. Al-Attar, K. Abdullah, V. Jankus, M. R. Bryce and A. P. Monkman, *Angewandte Chemie*, 2014, **126**, 11800-11803.
20. A. Tronnier and T. Strassner, *Dalton Transactions*, 2013, **42**, 9847-9851.
21. A. M'hamedj, M. A. Fox, A. S. Batsanov, H. A. Al-Attar, A. P. Monkman and M. R. Bryce, *Journal of Materials Chemistry C*, 2017, **5**, 6777-6789.
22. X. Yang, B. Jiao, J.-S. Dang, Y. Sun, Y. Wu, G. Zhou and W.-Y. Wong, *ACS Applied Materials & Interfaces*, 2018, **10**, 10227-10235.
23. J. Zhang, L. Zhou, H. A. Al-Attar, K. Shao, L. Wang, D. Zhu, Z. Su, M. R. Bryce and A. P. Monkman, *Advanced Functional Materials*, 2013, **23**, 4667-4677.
24. Q. B. Pei, G. Yu, C. Zhang, Y. Yang and A. J. Heeger, *Science*, 1995, **269**, 1086-1088.
25. J. K. Lee, D. S. Yoo, E. S. Handy and M. F. Rubner, *Applied Physics Letters*, 1996, **69**, 1686-1688.
26. G. Y. Chen, B. R. Chang, T. A. Shih, C. H. Lin, C. L. Lo, Y. Z. Chen, Y. X. Liu, Y. R. Li, J. T. Guo, C. W. Lu, Z. P. Yang and H. C. Su, *Chem.-Eur. J.*, 2019, **25**, 5489-5497.
27. J. Park, K. Shanmugasundaram, J. C. John and Y. Choe, *J. Photochem. Photobiol. A-Chem.*, 2019, **374**, 10-15.

28. M. Diethelm, Q. Grossmann, A. Schiller, E. Knapp, S. Jenatsch, M. Kawecki, F. Nuesch and R. Hany, *Adv. Opt. Mater.*, 2019, **7**, 8. View Article Online
DOI: 10.1039/C9TC02930C
29. D. A. W. Ross, P. A. Scattergood, A. Babaei, A. Pertegás, H. J. Bolink and P. I. P. Elliott, *Dalton Transactions*, 2016, **45**, 7748-7757.
30. A. Sandström and L. Edman, *Energy Technology*, 2015, **3**, 329-339.
31. G. Hernandez-Sosa, S. Tekoglu, S. Stolz, R. Eckstein, C. Teusch, J. Trapp, U. Lemmer, M. Hamburger and N. Mechau, *Advanced Materials*, 2014, DOI: 10.1002/adma.201305541, 3235-3240.
32. A. Sandström, H. F. Dam, F. C. Krebs and L. Edman, *Nature Communications*, 2012, **3**, 1002.
33. A. Sandström, A. Asadpoordarvish, J. Enevold and L. Edman, *Advanced Materials*, 2014, **26**, 4975-4980.
34. E. M. Lindh, A. Sandström and L. Edman, *Small*, 2014, **10**, 4148-4153.
35. G. Mauthner, K. Landfester, A. Kock, H. Bruckl, M. Kast, C. Stepper and E. J. W. List, *Organic Electronics*, 2008, **9**, 164-170.
36. J. Zimmermann, S. Schliske, M. Held, J.-N. Tisserant, L. Porcarelli, A. Sanchez-Sanchez, D. Mecerreyes and G. Hernandez-Sosa, *Advanced Materials Technologies*, 2019, **4**, 1800641.
37. B. Nemati Bideh and H. Shahroosvand, *Scientific Reports*, 2017, **7**, 15739.
38. C.-C. Ju, C.-H. Chen, C.-L. Yuan and K.-Z. Wang, *Thin Solid Films*, 2011, **519**, 3883-3889.
39. J.-C. Leprêtre, A. Deronzier and O. Stéphan, *Synthetic Metals*, 2002, **131**, 175-183.
40. J. Fernández-Cestau, N. Giménez, E. Lalinde, P. Montañó, M. T. Moreno, S. Sánchez, M. D. Weber and R. D. Costa, *Dalton Transactions*, 2016, **45**, 3251-3255.
41. R. D. Costa, G. Fernández, L. Sánchez, N. Martín, E. Ortí and H. J. Bolink, *Chemistry – A European Journal*, 2010, **16**, 9855-9863.
42. Maria-Grazia La-Placa, Ana María Igual-Muñoz, Jorge Romero, Ruth E. Daniels, Valery N. Kozhevnikov, Michele Sessolo, a. H. J. Bolink and *ECS J. Solid State Sci. Technol.*, 2019, **8**, R84-R87.
43. L. M. Cinninger, L. D. Bastatas, Y. Shen, B. J. Holliday and J. D. Slinker, *Dalton Transactions*, 2019, **48**, 9684-9691.
44. G. Sheldrick, *Acta Crystallogr. A*, 2015, **71**, 3-8.
45. O. V. Dolomanov, L. J. Bourhis, R. J. Gildea, J. A. K. Howard and H. Puschmann, *J. Appl. Cryst.*, 2009, **42**, 339-341.
46. M. J. Frisch, G. W. Trucks, H. B. Schlegel, G. E. Scuseria, M. A. Robb, J. R. Cheeseman, G. Scalmani, V. Barone, B. Mennucci, G. A. Petersson, H. Nakatsuji, M. Caricato, X. Li, H. P. Hratchian, A. F. Izmaylov, J. Bloino, G. Zheng, J. L. Sonnenberg, M. Hada, M. Ehara, K. Toyota, R. Fukuda, J. Hasegawa, M. Ishida, T. Nakajima, Y. Honda, O. Kitao, H. Nakai, T. Vreven, J. A. Montgomery Jr., J. E. Peralta, F. Ogliaro, M. J. Bearpark, J. Heyd, E. N. Brothers, K. N. Kudin, V. N. Staroverov, R. Kobayashi, J. Normand, K. Raghavachari, A. P. Rendell, J. C. Burant, S. S. Iyengar, J. Tomasi, M. Cossi, N. Rega, N. J. Millam, M. Klene, J. E. Knox, J. B. Cross, V. Bakken, C. Adamo, J. Jaramillo, R. Gomperts, R. E. Stratmann, O. Yazyev, A. J. Austin, R. Cammi, C. Pomelli, J. W. Ochterski, R. L. Martin, K. Morokuma, V. G. Zakrzewski, G. A. Voth, P. Salvador, J. J. Dannenberg, S. Dapprich, A. D. Daniels, Ö. Farkas, J. B. Foresman, J. V. Ortiz, J. Cioslowski and D. J. Fox, *Gaussian 09*, Gaussian, Inc., Wallingford, CT, USA, 2009.
47. Y. Zhao and D. G. Truhlar, *Theor. Chem. Acc.*, 2008, **120**, 215-241.
48. F. Weigend and R. Ahlrichs, *Phys. Chem. Chem. Phys.*, 2005, **7**, 3297-3305.
49. F. Weigend, *Phys. Chem. Chem. Phys.*, 2006, **8**, 1057-1065.
50. Y. Zhao and D. G. Truhlar, *The Journal of Chemical Physics*, 2006, **125**, 194101.
51. M. Cossi, N. Rega, G. Scalmani and V. Barone, *J. Comput. Chem.*, 2003, **24**, 669-681.
52. G. Baryshnikov, B. Minaev and H. Ågren, *Chem. Rev.*, 2017, **117**, 6500-6537.
53. M. Montalti, A. Credi, L. Prodi and M. T. Gandolfi, *Handbook of Photochemistry, Third Edition*, CRC Press, 2006.
54. H. Yersin, ed., *Highly Efficient OLEDs with Phosphorescent Materials*, Wiley-VCH, Weinheim, 2008.

55. N. J. Turro, V. Ramamurthy and J. C. Scaiano, *Modern Molecular Photochemistry of Organic Molecules*, University Science Books, Sausalito, 2010. View Article Online
DOI: 10.1039/C9TC02930C
56. A. F. Rausch, H. H. H. Homeier and H. Yersin, *Top. Organomet. Chem.*, 2010, **29**, 193-235.
57. H. Yersin, A. F. Rausch, R. Czerwieniec, T. Hofbeck and T. Fischer, *Coord. Chem. Rev.*, 2011, **255**, 2622-2652.
58. J. Brooks, Y. Babayan, S. Lamansky, P. I. Djurovich, I. Tsyba, R. Bau and M. E. Thompson, *Inorg. Chem.*, 2002, **41**, 3055-3066.
59. N. M. Shavaleev, H. Adams, J. Best, R. Edge, S. Navaratnam and J. A. Weinstein, *Inorg. Chem.*, 2006, **45**, 9410-9415.
60. G. Turnbull, J. A. G. Williams and V. N. Kozhevnikov, *Chem. Commun.*, 2017, **53**, 2729-2732.
61. A. M. Bünzli, H. J. Bolink, E. C. Constable, C. E. Housecroft, J. M. Junquera-Hernández, M. Neuburger, E. Ortí, A. Pertegás, J. J. Serrano-Pérez, D. Tordera and J. A. Zampese, *Dalton Trans.*, 2014, **43**, 738-750.
62. A. F. Henwood and E. Zysman-Colman, *Top. Curr. Chem.*, 2016, **374**, 36.
63. T. Hofbeck and H. Yersin, *Inorg. Chem.*, 2010, **49**, 9290-9299.
64. M. Z. Shafikov, R. Daniels, P. Pander, F. B. Dias, J. A. G. Williams and V. N. Kozhevnikov, *ACS Appl. Mater. Interfaces*, 2019, **11**, 8182-8193.
65. L. F. Gildea and J. A. G. Williams, in *Organic light-emitting diodes: materials, devices and applications*, ed. B. A., Woodhead Publishing, Cambridge, 2013, pp. 77-113.
66. R. Englman and J. Jortner, *Mol. Phys.*, 1970, **18**, 145-164.
67. L.-S. Cui, Y. Liu, X.-Y. Liu, Z.-Q. Jiang and L.-S. Liao, *ACS Appl. Mater. Interfaces*, 2015, **7**, 11007-11014.
68. J. S. Griffith, *The Theory of Transition-Metal Ions*, Cambridge University Press, 1964.
69. F. Neese, *J. Chem. Phys.*, 2007, **127**, 164112.
70. F. Neese, *Journal of the American Chemical Society*, 2006, **128**, 10213-10222.
71. A. F. Rausch, M. E. Thompson and H. Yersin, *Inorg. Chem.*, 2009, **48**, 1928-1937.
72. R. Czerwieniec, T. Hofbeck, O. Crespo, A. Laguna, M. Concepción Gimeno and H. Yersin, *Inorg. Chem.*, 2010, **49**, 3764-3767.
73. G. D. Hager and G. A. Crosby, *J. Amer. Chem. Soc.*, 1975, **97**, 7031-7037.
74. T. Azumi, C. M. O'Donnell and S. P. McGlynn, *J. Chem. Phys.*, 1966, **45**, 2735-2742.
75. W. J. Finkenzeller and H. Yersin, *Chem. Phys. Lett.*, 2003, **377**, 299-305.
76. P. Matyba, K. Maturova, M. Kemerink, N. D. Robinson and L. Edman, *Nature Materials*, 2009, **8**, 672-676.
77. S. Y. Hu and J. Gao, *Electrochimica Acta*, 2019, **304**, 184-191.
78. S. Tang, P. Murto, X. Xu, C. Larsen, E. Wang and L. Edman, *Chemistry of Materials*, 2017, **29**, 7750-7759.
79. M. A. Baldo, C. Adachi and S. R. Forrest, *Physical Review B*, 2000, **62**, 10967-10977.
80. T. Yasuda, Y. Yamaguchi, D.-C. Zou and T. Tsutsui, *Japanese Journal of Applied Physics*, 2002, **41**, 5626-5629.
81. S. Tang, A. Sandström, P. Lundberg, T. Lanz, C. Larsen, S. van Reenen, M. Kemerink and L. Edman, *Nature Communications*, 2017, **8**, 1190.
82. S. Tang and L. Edman, *Topics in Current Chemistry*, 2016, **374**, 40.
83. J. Mindemark, S. Tang, J. Wang, N. Kaihovirta, D. Brandell and L. Edman, *Chemistry of Materials*, 2016, **28**, 2618-2623.
84. S. van Reenen, T. Akatsuka, D. Tordera, M. Kemerink and H. J. Bolink, *Journal of the American Chemical Society*, 2013, **135**, 886-891.
85. R. D. Costa, E. Orti, H. J. Bolink, F. Monti, G. Accorsi and N. Armaroli, *Angew. Chem.-Int. Edit.*, 2012, **51**, 8178-8211.
86. E. Zysman-Colman, J. D. Slinker, J. B. Parker, G. G. Malliaras and S. Bernhard, *Chemistry of Materials*, 2008, **20**, 388-396.
87. J. Gao, *Curr. Opin. Electrochem.*, 2018, **7**, 87-94.